

# Translation-equivariant Image Quantizer for Bi-directional Image-Text Generation

Woncheol Shin<sup>1</sup> Gyubok Lee<sup>1</sup> Jiyoung Lee<sup>1</sup> Joonseok Lee<sup>2,3</sup> Edward Choi<sup>1</sup>

<sup>1</sup>KAIST <sup>2</sup>Google Research <sup>3</sup>Seoul National University

<sup>1</sup>{swc1905, gyubok.lee, jiyounglee0523, edwardchoi}@kaist.ac.kr <sup>2</sup>joonseok2010@gmail.com

## Abstract

Recently, vector-quantized image modeling has demonstrated impressive performance on generation tasks such as text-to-image generation. However, we discover that the current image quantizers do not satisfy translation equivariance in the quantized space due to aliasing, degrading performance in the downstream text-to-image generation and image-to-text generation, even in simple experimental setups. Instead of focusing on anti-aliasing, we take a direct approach to encourage translation equivariance in the quantized space. In particular, we explore a desirable property of image quantizers, called ‘Translation Equivariance in the Quantized Space’ and propose a simple but effective way to achieve translation equivariance by regularizing orthogonality in the codebook embedding vectors. Using this method, we improve accuracy by +22% in text-to-image generation and +26% in image-to-text generation, outperforming the VQGAN.

## 1. Introduction

Unlike previous works that directly predict pixel values [4, 22, 29], recent autoregressive image generation approaches adopt vector quantization and achieve high-quality generation performance [7, 25]. In particular, DALL-E [25] demonstrates impressive zero-shot text-conditioned image generation, only using image quantization and Transformer network [31]. Similar to theirs, methods that utilize vector quantization in image downstream tasks mainly take a two-stage approach: quantization and quantized image modeling. As its initial step, an image quantizer (e.g., VQ-VAE [28] or VQGAN [7]) encodes an image as a sequence of codebook indices using codebook embeddings. Then, the resulting indices are given as input to downstream image modeling tasks. By modeling images in this fashion, the input indices of the downstream task can be treated the same as token indices in text. This discretization of images allows us to take advantage of training with a classification

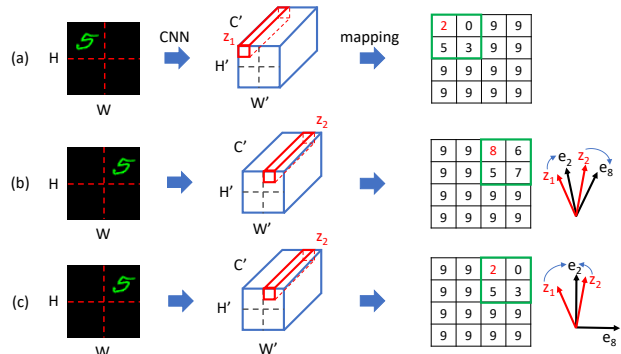


Figure 1. (a) Image quantization before translation of the top-left 5; (b) Broken translation equivariance in the quantized space after the translation of 5; (c) Perfect translation equivariance in the quantized space with our orthogonal codebook embeddings. Note that  $e_2, e_8 \in \mathbb{R}^{C'}$  are the closest codebook embedding vectors to  $z_1, z_2 \in \mathbb{R}^{C'}$ , where  $z_1, z_2$  are the corresponding feature map fibers in terms of shifted location. By enforcing orthogonality in the quantized space as in (c), a slight deviation due to aliasing can be ignored, and the same codebook index (e.g. 2) is given to  $z_1, z_2$ .

objective, to model a relatively shorter sequence of image representations, and to even jointly handle textual information more naturally.

While the machine learning community appreciates vector quantization in image modeling lately, we discover that the existing quantization method breaks a desirable property of *translation equivariance* in the quantized space. As shown in Fig. 1 (b), the resulting indices of an image patch on the top left corner turn out to be not identical to those on the top right corner when using the vanilla VQGAN [7]. Furthermore, this phenomenon in the current image quantization methods severely hinders the downstream image-to-text and text-to-image generation tasks—one of challenging but immediately applicable multimodal learning problems—even in a relatively simple experimental setup.

Referring to the literature, the cause of the broken translation equivariance is due to aliasing, caused by down-

sampling operations (*e.g.*, strided convolution, maxpooling) [27, 37]. In other words, the following can hold:

$$z_2 = z_1 + \epsilon,$$

where  $\epsilon$  is a noise caused by aliasing, and  $z_1$  and  $z_2$  are the corresponding feature maps in terms of the shifted location (Fig. 1). In an effort to reduce  $\epsilon$ , one of the anti-aliasing methods in both signal processing and CNNs is to apply a low-pass filter during downsampling [10, 14, 23, 37]. However, in deep neural networks, it is challenging to enforce  $\epsilon$  to be completely zero in the feature map space, as complete anti-aliasing still requires careful manipulation of filters. However, when it comes to image quantization, where images are represented as codebook indices,  $\epsilon$  no longer needs to be zero as long as the feature map fibers are mapped to the same codebook index. This implies that translation equivariance in the quantized space can be achieved by a different approach than enforcing translation equivariance in the image feature map space.

In this paper, we first explore *translation equivariance in the image quantized space* and propose a simple and effective way to achieve translation equivariance by enforcing orthogonality among the codebook embeddings. To show the effectiveness of our method in translation equivariance (TE), we implement an orthogonality-regularized VQGAN (*TE-VQGAN*), and a bi-directional image-text generator (roughly put, ‘*Bi-directional DALL-E*’). Using the proposed method, we empirically demonstrate that the translation-equivariant image quantizer dramatically improves generalization ability and sample efficiency of image-to-text and text-to-image generation in zero-shot-like setups (*e.g.*, modeling objects in an unseen location).

Our contributions are summarized as the following:

- To the best of our knowledge, we first explore the problem of *translation equivariance in the image quantized space*.
- Instead of focusing on anti-aliasing, we take a direct approach to achieve translation equivariance in the quantized space by regularizing orthogonality in the codebook embedding vectors.
- We show that a translation-equivariant image quantizer improves the accuracy of text-to-image and image-to-text generation on text-augmented MNIST by up to +22% and +26%, respectively. We discuss insights discovered from our analysis on the behavior of the quantized representations.

## 2. Related Work

**Image Quantization.** Image quantization or vector quantization of images is an efficient encoding method that represents images in the discrete latent space via an encoder and decoder. Images, by their nature, contain many correlated pixels and noise, and therefore representing images

in the pixel space may contain redundant information [28]. By encoding images in a quantized manner, downstream models can leverage training with a classification objective with a much shorter sequence of tokens, which are limited when dealing with pure pixels. Starting from VQVAE [28], Esser *et al.* proposed an effective extension of VQVAE (VQGAN) [7] by introducing an adversarial loss and perceptual loss. The addition of two objectives provides image representations that result in a sharper and detailed reconstruction of images. More recently, Yu *et al.* further boosted the efficiency and reconstruction quality of image quantizers [36] with the ViT architecture [6], replacing CNNs. In this paper, we utilize VQGAN as our base image quantizer to explore the behaviors of translation equivariance in the image quantized space.

**Translation Invariance & Equivariance.** The modern convolutional networks take advantage of the property of translation invariance and equivariance. Translation invariance requires the output unchanged by the shifts in the input, while translation equivariance is a mapping which, when the input is shifted, leads to a shifted output. In other words, translation invariance is about the final representation after Global Average Pooling (GAP) in CNNs, and translation equivariance is about the feature map before GAP. A fundamental approach to handle translation invariance and equivariance is anti-aliasing. Classically, Simoncelli *et al.* [27] first formalized ‘shiftability’ and related it to aliasing. Since then, careful calibration of sampling rate according to the Nyquist sampling theorem [21] or applying a low-pass filter has been a natural choice to avoid aliasing in downsampling.

It is only recently that deep learning has started to explore translation invariance and equivariance [1, 30, 37, 40]. Zhang [37] applied a low pass filter between a stride-one operator and naive subsampling to improve translation equivariance in the latent feature map space, but Azulay *et al.* [1] pointed out that nonlinearity such as ReLU still hinders anti-aliasing even with low-pass filtering. Karras *et al.* [14] proposed an ideal sampling method and nonlinearity to avoid aliasing and achieved translation equivariance in the image generation task. In a similar motivation to theirs, we investigate translation equivariance in the generation task but pay special attention to the vector-quantized space and multimodal learning problem.

**Image  $\rightarrow$  Text & Text  $\rightarrow$  Image Generation.** *Multimodal translation or generation* is a long-studied problem. Recently, the advances in computer vision and NLP shed light on the interest of multimodal generation, and it has been utilized as a testbed for multiple aspects of learning algorithms [2]. The simplest and popular forms of multimodal generation are image-to-text and text-to-image generation. Image-to-text generation (*I  $\rightarrow$  T generation* or image captioning) is a task that takes an image input and generates

coherent natural language descriptions according to the image content. Conversely, text-to-image generation ( $T \rightarrow I$  generation) is a task that translates from text to image while preserving the text semantics and the coherence of generated images. Among various methods to tackle two separate tasks, self-attention has been the mainstream method that offers a unified framework to encode (and decode) both text and image data naturally [16–18, 25, 35, 39]. Some studies aimed to perform both generation tasks with a single model [5, 12], where K-means clustering was used to discretize the image features, leading to suboptimal image generation performance than using image quantization. In this work, to investigate the effectiveness of translation equivariance in the quantized space, we used the DALL-E architecture to conduct both  $I \rightarrow T$  and  $T \rightarrow I$  generation tasks.

### 3. Method

In this section, we first define the term *Translation Equivariance (TE) in the Quantized Space*. Then, we introduce our image quantizer by training VQGAN with our proposed method (*TE-VQGAN*), followed by the  $I \rightarrow T$  and  $T \rightarrow I$  generator (*Bi-directional DALL-E*) to show the effectiveness of our method.

#### 3.1. Translation Equivariance in Quantized Space

Let  $\mathbf{x} \in \mathbb{R}^{H \times W \times 3}$  be an input image of size  $H \times W$  with RGB channels. A convolutional neural network (CNN)  $\mathcal{F}$  takes this image  $\mathbf{x}$  as input, and produces a feature map  $\mathcal{F}(\mathbf{x}) \in \mathbb{R}^{H' \times W' \times C'}$ . Then, the function  $\mathcal{F}$  is called *translation-equivariant* if

$$\mathcal{F}(T_1(\mathbf{x})) = T_2(\mathcal{F}(\mathbf{x}))$$

where  $T_1$  is a translation operation in the image space and  $T_2$  is the translation operation in the feature map space corresponding to  $T_1$ .

Let  $Q$  be a quantization operation, and  $Q(\mathcal{F}(\mathbf{x})) = \mathcal{F}^q(\mathbf{x}) \in \mathbb{R}^{H' \times W' \times C'}$  be the quantized feature map.  $\mathcal{F}$  is called *translation equivariance in the quantized space* if,

$$\mathcal{F}^q(T_1(\mathbf{x})) = T_2(\mathcal{F}^q(\mathbf{x})).$$

In other words, it is enough for the translation equivariance in the quantized space to have the  $T_2$  relationship between the quantized code indices of  $\mathcal{F}(T_1(\mathbf{x}))$  and  $\mathcal{F}(\mathbf{x})$ , even if  $\mathcal{F}(T_1(\mathbf{x})) \neq T_2(\mathcal{F}(\mathbf{x}))$ . Note that we can safely focus only on the relationship between the code indices, because *Bi-directional DALL-E* in the following stage takes the input image in the form of code indices, not image feature maps or codebook embedding vectors.

#### 3.2. Model Architecture & Training

To show the advantage of translation-equivariant image encoding in the quantized space, we adopt a two-stage approach: a CNN-based image quantizer (Stage 1) followed by a unified decoder-only Transformer that performs both  $T \rightarrow I$  generation and  $I \rightarrow T$  generation (Stage 2).

##### 3.2.1 Stage 1: Image Quantizer (TE-VQGAN)

Our image quantizer is based on VQGAN [7]. VQGAN consists of a CNN-based encoder  $\mathcal{F}$ , a CNN-based decoder  $\mathcal{G}$ , a discriminator  $D$ , and codebook embeddings  $e \in \mathbb{R}^{C' \times K}$ , where  $K$  is the size of the codebook and  $C'$  is the number of feature channels.  $\mathcal{F}$  gets an input image  $\mathbf{x} \in \mathbb{R}^{H \times W \times 3}$  and produces a feature map  $\mathcal{F}(\mathbf{x}) \in \mathbb{R}^{H' \times W' \times C'}$ . Let  $d$  be the number of downsampling operations in the encoder, then  $H'$  and  $W'$  can be calculated as

$$H' = \frac{H}{2^d}, W' = \frac{W}{2^d}.$$

Let a fiber of the feature map whose spatial coordinate is  $(h', w')$  be  $\mathcal{F}(\mathbf{x})_{(h', w')} \in \mathbb{R}^{C'}$ , where  $(h', w') \in [1, H'] \times [1, W']$  and  $h', w' \in \mathbb{Z}$ .  $\mathcal{F}(\mathbf{x})_{(h', w')}$  is assigned to the closest embedding vector  $e_k \in \mathbb{R}^{C'}$  based on  $L_2$  distance:

$$\mathcal{F}^q(\mathbf{x})_{(h', w')} = e_k, \text{ where } k = \operatorname{argmin}_j \|\mathcal{F}(\mathbf{x})_{(h', w')} - e_j\|_2^2.$$

**Training.** Let  $\hat{\mathbf{x}}$  to denote the reconstructed image,  $\mathcal{G}(\mathcal{F}^q(\mathbf{x})) \in \mathbb{R}^{H \times W \times 3}$ . VQGAN, like its predecessor VQ-VAE [28], tries to maximize the similarity between the input  $\mathbf{x}$  and its reconstruction  $\hat{\mathbf{x}}$ . In addition, VQGAN uses a patch-based discriminator  $D$  [13] to increase the quality of  $\hat{\mathbf{x}}$  by playing an adversarial game between discriminator  $D$  and the generator (encoder  $\mathcal{F}$ , decoder  $\mathcal{G}$ , embedding  $e$ ). The objective function of VQGAN is

$$\min_{\mathcal{F}, \mathcal{G}, e} \max_D \mathbb{E}_{\mathbf{x} \sim p(\mathbf{x})} [\mathcal{L}_{\text{VQ}}(\mathcal{F}, \mathcal{G}, e) + \gamma \mathcal{L}_{\text{GAN}}(\{\mathcal{F}, \mathcal{G}, e\}, D)]$$

where

$$\begin{aligned} \mathcal{L}_{\text{GAN}}(\{\mathcal{F}, \mathcal{G}, e\}, D) &= \log D(\mathbf{x}) + \log(1 - D(\hat{\mathbf{x}})), \text{ and} \\ \mathcal{L}_{\text{VQ}}(\mathcal{F}, \mathcal{G}, e) &= \|\mathbf{x} - \hat{\mathbf{x}}\|_2^2 + \mathcal{L}_p \\ &\quad + \|\operatorname{sg}[\mathcal{F}(\mathbf{x})] - \mathcal{F}^q(\mathbf{x})\|_2^2 \\ &\quad + \beta \|\mathcal{F}(\mathbf{x}) - \operatorname{sg}[\mathcal{F}^q(\mathbf{x})]\|_2^2. \end{aligned} \quad (1)$$

Here,  $\operatorname{sg}[\cdot]$  is the stop-gradient operator, and  $\mathcal{L}_p$  is the perceptual loss [38] between  $\mathbf{x}$  and  $\hat{\mathbf{x}}$ .  $\gamma$  is calculated as follows [7]:

$$\gamma = \frac{\nabla_{\mathcal{G}} \left[ \|\mathbf{x} - \hat{\mathbf{x}}\|_2^2 + \mathcal{L}_p \right]}{\nabla_{\mathcal{G}} [\mathcal{L}_{\text{GAN}}] + \delta},$$

where  $\nabla_{\mathcal{G}}[\cdot]$  denotes the gradient of its input with regards to the last layer of the decoder  $\mathcal{G}$ . Note that the gradient back-propagation cannot reach to the encoder because of the non-differentiable operation  $\mathcal{F}^q(\cdot)$ . For that problem, we simply copy the gradients from the first layer of the decoder  $\mathcal{G}$  to the last layer of the encoder  $\mathcal{F}$  [28].

As mentioned in Sec. 1, if we interpret alias as a noise due to downsampling, the following relationship may hold:

$$\mathcal{F}(T_1(\mathbf{x}))_{(h', w')} = T_2(\mathcal{F}(\mathbf{x}))_{(h', w')} + \epsilon,$$

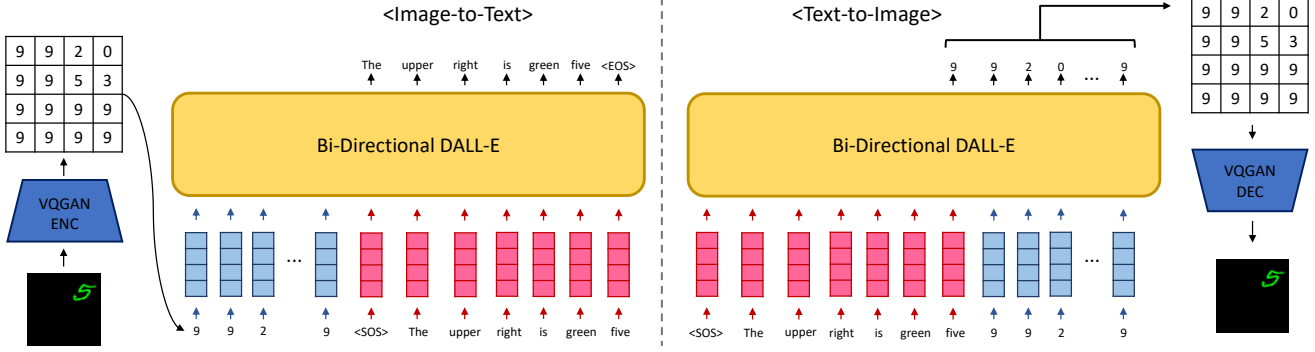


Figure 2. Bi-Directional DALL-E Architecture. In Image-to-Text generation, the model receives quantized image indices produced by pre-trained VQGAN encoder as inputs and generates corresponding text. In Text-to-Image generation, the model receives text as input and generates quantized image indices which later pass through pre-trained VQGAN decoder to produces a corresponding image. We used separate embeddings for each modality; red indicates text embedding and blue indicates image quantized indices embedding.

Here, it is a non-trivial task to make  $\epsilon$  zero. However, as mentioned in Sec. 3.1, as long as we are only interested in the image code indices, we can focus on assigning the same code embedding  $e_k$  to both  $\mathcal{F}(T_1(\mathbf{x}))_{(h',w')}$  and  $T_2(\mathcal{F}(\mathbf{x}))_{(h',w')}$  rather than trying to make  $\epsilon = 0$ . Surprisingly, this can be achieved by simply enforcing the orthogonal structure in the quantized space; that is, by regularizing the embedding vectors  $e_k$  to be orthogonal to each other. The intuition behind this is well illustrated in Fig. 1. In the unregularized quantized space, feature maps  $z_1$  and  $z_2$  that slightly differ due to alias are mapped to respective embedding vectors  $e_2$  and  $e_8$ , respectively. In the orthogonal quantized space, however, every embedding vector is orthogonal to one another, and it is easier to ignore small noise due to alias when  $z_1$  and  $z_2$  are mapped to the same embedding vector  $e_2$ .

We add the following regularization term to Eq. (1) to enforce orthogonality among the codebook embeddings:

$$\mathcal{L}_{\text{REG}}(e) = \lambda \frac{1}{K^2} \|\ell_2(e)^\top \ell_2(e) - I\|_F^2 \quad (2)$$

where  $\ell_2(e) \in \mathbb{R}^{C' \times K}$  denotes an  $L_2$ -normalized code embedding along the first dimension. Note that we do not enforce  $e_k$ 's to be orthonormal, which was used in other studies [3], since orthonormal embedding vectors will drive the norm of feature fibers  $\mathcal{F}(\mathbf{x})_{(h',w')}$  to 1 due to the third term in Eq. (1), thereby limiting the expressiveness of the CNN encoder. We report detailed comparison of the two approaches in Appendix C to show that forcing orthonormality indeed decreases performance.

On a last note, although we use VQGAN in this work, this regularization can be applied to any codebook-based image quantizers.

### 3.2.2 Stage 2: Bi-directional DALL-E

We adopt the architecture of DALL-E [25] to test the effect of our proposed method in both  $T \rightarrow I$  generation and  $I \rightarrow$

$T$  generation.

Let an image and text description pair be  $(\mathbf{x}, \mathbf{t})$ . First we convert  $\mathbf{x}$  to a matrix of codebook indices  $\mathbf{S} \in \{0, 1, \dots, K-1\}^{H' \times W'}$  using a pretrained image quantizer, and  $\mathbf{t}$  to a sequence of subword indices  $\mathbf{T} \in \{0, 1, \dots, |\mathcal{V}|-1\}^L$  with a BPE tokenizer [26], where  $\mathcal{V}$  is the vocabulary set and  $L$  is the maximum subword length. Note that *Bi-directional DALL-E* is given only the code indices (not codebook embedding vectors) for the image. Therefore, the visual feature embedding  $\mathbf{v} = [\mathbf{v}_{(0,0)}, \mathbf{v}_{(0,1)}, \dots, \mathbf{v}_{(H'-1, W'-1)}]$  is formed using the codebook-indices matrix  $\mathbf{S}$ :

$$\mathbf{v}_{(h',w')} = VE(\mathbf{S}_{(h',w')}) + PE(h', w'),$$

where  $VE: \mathbb{Z} \rightarrow \mathbb{R}^{C'}$  is the lookup function from codebook index to its corresponding token embedding, and  $PE: \mathbb{Z} \times \mathbb{Z} \rightarrow \mathbb{R}^{C'}$  is the lookup function for 2-D sinusoidal positional encoding [33] at the given row and column index. The language feature embedding  $\mathbf{w} = [\mathbf{w}_1, \mathbf{w}_2, \dots, \mathbf{w}_L]$  is formed similarly:

$$\mathbf{w}_i = WE(\mathcal{T}_i) + LPE(i)$$

where  $WE: \mathbb{Z} \rightarrow \mathbb{R}^{C'}$  is the word embedding lookup function, and  $LPE: \mathbb{Z} \rightarrow \mathbb{R}^{C'}$  is the lookup operation for learnable positional encoding [9]. We concatenate  $\mathbf{w}$  and  $\mathbf{v}$  to construct the final input sequence. *Bi-directional DALL-E* takes  $[\mathbf{w}; \mathbf{v}]$  as input and uses the mask types from [25] for text-to-image generation. Note that we concatenate them in a reverse order (e.g.,  $[\mathbf{v}; \mathbf{w}]$ ) for image-to-text generation and use slightly different mask types accordingly to the reverse order. The details of the mask types are in Appendix A.

**Training.** We train *Bi-directional DALL-E* with autoregressive next-index prediction.  $T \rightarrow I$  generation aims to maximize the likelihood of the observed codebook index sequence given the subword index sequence. Therefore, we use the following loss function:



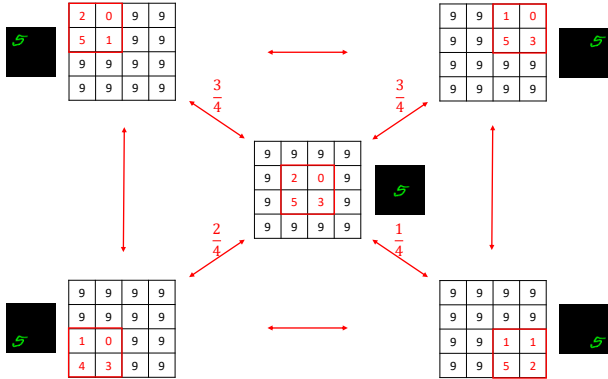


Figure 3. Translation equivariance accuracy. In this example, ‘Trans-eq acc’ =  $\text{Mean}(\frac{3}{4}, \frac{3}{4}, \frac{2}{4}, \frac{1}{4}, \dots)$ .

$$\mathcal{L}_{T \rightarrow I}(\theta) = -\mathbb{E}_{(\mathbf{x}, \mathbf{t}) \sim D} \left[ \sum_i \log P_{\theta}(\mathbf{S}_i | \mathbf{T}, \mathbf{S}_{<i}) \right] \quad (3)$$

where  $\theta$  is the trainable parameters of the *Bi-directional DALL-E*, and  $\mathbf{S}_i$  is the  $i$ -th element of the matrix  $\mathbf{S}$  when we read it in a raster scan order. A pair of image and its corresponding text  $(\mathbf{x}, \mathbf{t})$  is sampled from the train set  $D$ .

$I \rightarrow T$  generation, conversely, aims to learn the likelihood of the subword index sequence given the codebook index sequence:

$$\mathcal{L}_{I \rightarrow T}(\theta) = -\mathbb{E}_{(\mathbf{x}, \mathbf{t}) \sim D} \left[ \sum_i \log P_{\theta}(\mathbf{T}_i | \mathbf{S}, \mathbf{T}_{<i}) \right] \quad (4)$$

For each training iteration, we alternate between  $T \rightarrow I$  and  $I \rightarrow T$ . Following DALL-E’s training strategy, when using Eq. (3), we also make the model predict the next subword indices in addition to predicting the next image codebook indices in 1:7 ratio, and vice versa when using Eq. (4). Further training details are provided in Appendix A.

## 4. Experiments

We first demonstrate the proposed method improves translation equivariance in the quantized space, using an MNIST-based dataset. Then we show this leads to improved performance in both  $I \rightarrow T$  and  $T \rightarrow I$  generation. Lastly, we perform additional experiments on another dataset (Fashion-MNIST) based on the findings in the previous experiments. All materials including codes and data are available at <https://github.com/wcshin-git/TE-VQGAN>.

### 4.1. Translation Equivariant Image Quantization

**Data Construction.** We use MNIST images to construct a dataset to test translation equivariance of image quantizers. First we sample one to four digits from the original dataset, and randomly place them in four quadrants of the  $64 \times 64$  space. Note that the original samples have the  $28 \times 28$  resolution, so we pad every sample with 2 pixels. Additionally, we sometimes sample only one digit and place it in

the center of the  $64 \times 64$  space. We call this dataset *Stage 1 Dataset* (examples shown in Appendix B). We prepare another dataset, called *Translated Dataset*, to measure the quantizer’s performance of *translation-equivariance in the quantized space*. This dataset only consists of single-digit images, copied five times for each place in the  $64 \times 64$  space. Each digit in the two datasets is colored in one of four colors (white, red, green and blue) for diverse experiments in Stage 2.

**Evaluation Metric for Translation Equivariance in the Quantized Space.** We use the *Translated Dataset* to measure the *translation equivariance in the quantized space*. The ‘translation equivariance accuracy’, shortened as ‘Trans-eq acc’, is defined as average accuracy of translation between all possible combinations of 5 regions in Fig. 3:

$$\text{Trans-eq acc} = \frac{\sum_{i < j} \text{Acc}_{ij}}{5C_2},$$

where  $\text{Acc}_{ij}$  measures the ratio of unchanged codebook indices between each corresponding position  $(h, w)$  from region  $r_i$  and  $r_j$ , that is,

$$\text{Acc}_{ij} = \frac{\sum_{h=1}^{\frac{H'}{2}} \sum_{w=1}^{\frac{W'}{2}} \mathbb{I}(\mathbf{S}[r_i]_{(h,w)} = \mathbf{S}[r_j]_{(h,w)})}{\frac{H'}{2} \times \frac{W'}{2}}$$

where  $\mathbf{S}[r_i]$  indicates the cropped matrix of codebook indices corresponding to the region  $i$  of the 5 locations in Fig. 3, and  $\mathbb{I}(\cdot)$  is 1 if the condition is true, and 0 otherwise.

**Experiment Setting.** We conducted a hyperparameter search to find the proper  $\lambda$  in Eq. (2). We explored 1, 10, 100, and 1000 as candidates, and found that  $\lambda = 10$  had the lowest validation  $\mathcal{L}_{VQ}$ . We also checked that the orthogonality regularization indeed makes the codebook embedding orthogonal when  $\lambda = 10$ . Therefore, we set  $\lambda$  to 10 and conducted all following experiments. Given the input resolution of  $64 \times 64$ , we downsampled twice in the VQGAN’s encoder. We set the dimension of the codebook embedding to 256. Therefore, the shape of the feature map  $\mathcal{F}(\mathbf{x})$  is  $16 \times 16 \times 256$ . To prevent noise derived by the image borders, we use the `ReplicationPad2d` in Pytorch [24] which pads the input tensor using replication of the input boundary. We set  $\beta$  in Eq. (1) to 0.25 following VQVAE [28]. Learning rate is fixed to  $8.0 \times 10^{-6} \times \text{batch size}$ , and we trained the image quantizer for 40 epochs via Adam optimizer [15] with  $\beta_1 = 0.5$  and  $\beta_2 = 0.9$ . All experiments are conducted three times varying the seed number.

#### 4.1.1 Varying Downsampling Method

Since aliasing occurs during downsampling, we test four different downsampling methods, including the Blurpool methods proposed by [37] to cope with alias: `StridedConv(SC)`, `ConvBlurpool(CB)`, `MaxPool(MP)`, and `MaxBlurpool(MB)`.

Method	Baseline	Ours
SC	0.874 (0.034)	0.970 (0.010)
CB	0.760 (0.027)	0.948 (0.023)
MP	0.779 (0.015)	0.970 (0.028)
MB	0.720 (0.019)	0.916 (0.009)

Table 1. Mean and standard deviation of ‘Trans-eq acc’ for each downsampling method. ‘Baseline’ are experiments without orthogonality, and ‘Ours’ are experiments with orthogonality.

We observe that the orthogonality regularization term improves ‘Trans-eq acc’ across all downsampling method. Note that Bluepool(CB, MB) [37] has not been able to improve its performance. We speculate that non-linearity functions, such as ReLU, make arbitrarily high frequencies which Blurpool tries to remove. Therefore, blurring before subsampling does not guarantee translation equivariance when nonlinearities exist [1, 14].

#### 4.1.2 Varying Codebook Size

Codebook size	Baseline	Ours
32	0.910 (0.025)	0.971 (0.010)
64	0.902 (0.031)	0.973 (0.005)
128	0.874 (0.034)	0.970 (0.010)
256	0.852 (0.023)	0.976 (0.006)

Table 2. Mean and standard deviation of ‘Trans-eq acc’ for each codebook size.

We fix the downsampling method as SC for further experiments, since it shows the best performance in the previous experiment. Here, we conduct experiments while changing the codebook size. For Baseline, ‘Trans-eq acc’ decreases as the codebook size increases. On the other hand, in our model, we observed consistent ‘Trans-eq acc’ across all codebook sizes. Also, we can check that standard deviation of the baseline is larger than that of ours, which indicates that the baseline model is highly unstable and sensitive to the seed number. In contrast, our model continually shows consistent result not affected by the seed numbers.

## 4.2. Image-Text Multimodal Generation

**Data Construction.** To train our *Bi-directional DALL-E*, we generated image captions where syntactic variation was added by changing the order of words, as demonstrated in Fig. 4. To perform zero-shot-like generation, we applied different constraints between the train and test set, as shown in Fig. 5. For example, white 0 on the upper left does not exist in the train set, while all 0’s in the test set are white and placed in upper left. We conjecture that the color constraint will not be as sensitive to translation equivariance as the digit constraint, since the former is less associated with shape. In total, we generated 300K samples for train, 3,000

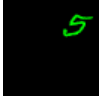
Figure	Caption
	The upper right is green five.
	The upper right five is green.
	The green number on the upper right is five.
	The green five is on the upper right.
	The five on the upper right is green.

Figure 4. Example of possible captions in *Stage 2 Dataset*. Five variants are available for a single digit. Furthermore, The word ‘upper’ and ‘lower’ can be changed to ‘top’ and ‘bottom’, respectively. For multi-digit samples, each digit has its own caption, and the order of the digit-specific captions are randomly determined.

		test set: ✓									
color	label	0	1	2	3	4	5	6	7	8	9
White		✓	✓	✓							
Red					✓	✓	✓				
Green								✓	✓		
blue										✓	✓

location	label	0	1	2	3	4	5	6	7	8	9
Upper Left		✓	✓	✓							
Upper Right					✓	✓	✓				
Lower Left								✓	✓		
Lower Right										✓	✓

Figure 5. *Stage 2 Dataset*: constraints of train and test set.

for validation, and 3,000 for test set. We call this *Stage 2 Dataset*. Illustrated examples can be found in Appendix B.

**Experiment Setting.** In Stage 2, *Bi-directional DALL-E* has 8 layers, 8 heads, and 64 head dimension. We train a BPE tokenizer [26] with our *Stage 2 Dataset* to split the text description into subwords with maximum length of 50<sup>1</sup>. Adam optimizer [15] is used with  $\beta_1 = 0.9$  and  $\beta_2 = 0.99$ , with cosine annealing learning rate scheduling [19] from 0.0 to  $1.0 \times 10^{-3}$ . We trained all models for 20 epochs. We compare the multimodal generation performance of Bi-directional DALL-E between using vanilla VQGAN (‘Baseline’) and using TE-VQGAN (‘Ours’).

#### 4.2.1 T → I Generation

In Text-to-Image (T → I), a model should generate an image that expresses the semantics of the given text. To evaluate this, we use a Resnet-18 [11] classifier on the generated images to classify color and digit. This classifier was pre-trained on our colored MNIST ( $28 \times 28$  resolution) to achieve 99.5% accuracy for digit and 100% for color. We cropped a digit of size  $28 \times 28$  from each quadrant of the generated images of size  $64 \times 64$  to use the pre-trained classifier. We evaluate the model on two test sets: 1) with the same constraint as the train set, denoted as ‘Seen’ 2) with a different constraint than the train set, denoted as

<sup>1</sup>The number of actively used unique subwords is 24.

‘Unseen’. We decoded the quantized image indices using top- $k$  sampling [8] where  $k = 0.1 \times (\text{codebook size} + \text{word vocab size})$ .

We measured the digit accuracy when the generated image had one (‘Quad1’), two (‘Quad2’), three (‘Quad3’), and four digits (‘Quad4’). Each case had about approximately 600 images. As an example, in Quad2, given a text ‘the lower right is blue nine, and the white two is on the upper left.’, a rule-based caption parser will convert the text into  $\{(LR, B, 9), (UL, W, 2)\}$ . With the parsed output, we crop the corresponding locations, lower right and upper left, from the generated image. Then, we use the pre-trained classifier on two cropped images and predict the digit and color. If the predicted digit or color are correct, this leads to increased accuracy.

Quad1	Seen		Unseen	
	Baseline	Ours	Baseline	Ours
SC	0.926 (0.011)	0.955 (0.013)	0.812 (0.032)	0.931 (0.033)
CB	0.942 (0.012)	0.961 (0.006)	0.753 (0.037)	0.923 (0.027)
MP	0.935 (0.011)	0.967 (0.003)	0.713 (0.007)	0.934 (0.043)
MB	0.939 (0.023)	0.934 (0.003)	0.724 (0.033)	0.900 (0.026)

Table 3. Digit accuracy of generated images in Quad1.

Quad4	Seen		Unseen	
	Baseline	Ours	Baseline	Ours
SC	0.926 (0.011)	0.949 (0.011)	0.761 (0.051)	0.868 (0.059)
CB	0.937 (0.003)	0.957 (0.004)	0.649 (0.055)	0.883 (0.043)
MP	0.936 (0.006)	0.959 (0.005)	0.656 (0.028)	0.851 (0.106)
MB	0.932 (0.025)	0.902 (0.004)	0.620 (0.077)	0.763 (0.054)

Table 4. Digit accuracy of generated images in Quad4.

Tab. 3 and Tab. 4 show the digit accuracy of text-to-image generation for Quad1 and Quad4, respectively. The results for Quad2 and Quad3 are provided in Appendix D.2, as well as samples generated by the model in Appendix D.4. We can see that the Baseline suffers a significant performance drop when moving from ‘Seen’ to ‘Unseen’. Using the orthogonality regularization, on the other hand, undergoes a dramatically smaller decrease, clearly demonstrating the importance of translation equivariance in the quantized space. Additionally, we can see that both Baseline and Ours have a harder time handling multiple ‘Unseen’ digits at once (Quad4). For color accuracy, as per our previous conjecture, both Baseline and Ours experienced negligible performance drop when moving from ‘Seen’ to ‘Unseen’ (99.9% accuracy to 99.8% accuracy), the detailed numbers are reported in Appendix D.2.

#### 4.2.2 I $\rightarrow$ T Generation

The model is given a  $64 \times 64$  image to generate a corresponding caption, which is evaluated by a rule-based parser

to calculate digit and color accuracy. For example, given a 3-digit image (Quad3), if the parsed triples of the true caption and the generated caption are  $\{(LR, B, 9), (UL, W, 2), (UR, R, 3)\}$ , and  $\{(UL, W, 5), (LR, B, 9)\}$ , the digit accuracy is  $1/3$  and the color accuracy is  $2/3$ .

Quad1	Seen		Unseen	
	Baseline	Ours	Baseline	Ours
SC	0.994 (0.002)	0.990 (0.007)	0.677 (0.022)	0.777 (0.041)
CB	0.994 (0.002)	0.995 (0.002)	0.475 (0.038)	0.623 (0.047)
MP	0.991 (0.002)	0.991 (0.003)	0.503 (0.024)	0.556 (0.072)
MB	0.991 (0.004)	0.991 (0.002)	0.503 (0.079)	0.763 (0.095)

Table 5. Digit accuracy of generated texts in Quad1.

Quad4	Seen		Unseen	
	Baseline	Ours	Baseline	Ours
SC	0.990 (0.003)	0.989 (0.001)	0.399 (0.026)	0.482 (0.079)
CB	0.993 (0.001)	0.991 (0.002)	0.242 (0.019)	0.325 (0.041)
MP	0.993 (0.001)	0.991 (0.001)	0.290 (0.026)	0.371 (0.052)
MB	0.992 (0.002)	0.992 (0.001)	0.299 (0.063)	0.437 (0.022)

Table 6. Digit accuracy of generated texts in Quad4.

Tab. 5 and Tab. 6 show the digit accuracy for Quad1 and Quad4, respectively. Similar to  $T \rightarrow I$  generation, we can see that the orthogonality regularization dramatically alleviates the performance drop issue when moving from ‘Seen’ to ‘Unseen’. Note that the ‘Unseen’ performance of  $I \rightarrow T$  generation is significantly lower than  $T \rightarrow I$  generation. We believe this comes from the difference between how text and image is evaluated. Since an image is classified as a whole, miss-predicting a code index or two might have little effect. But miss-predicting a specific text token, such as the digit token, can have a catastrophic impact. Closing the performance gap between the two directions is valuable future direction. The color accuracy is reported in Appendix D.3, where we can observe the same pattern as in  $T \rightarrow I$  generation. The generated samples are also found in Appendix D.4.

#### 4.3. New Dataset: Fashion-MNIST

To further explore the characteristics of image quantizers, we conduct similar experiments on another dataset, Fashion-MNIST [34]. Following the same data construction process as MNIST, we measure the performance of both translation equivariance and image-text generation with respect to orthogonality regularization. For image quantization, we fixed the downsampling method to SC and the codebook size to 128. We trained a Resnet classifier using our colored fashion-MNIST to classify item and color. The final performance of the classifier was 93.5% and 100% for fashion item and color, respectively.

In Tab. 7, TE-VQGAN shows 15% higher performance than vanilla-VQGAN in terms of ‘Trans-eq acc’. In Tab. 8,

	Baseline	Ours
SC, 128	0.791 (0.023)	0.941 (0.014)

Table 7. Mean and standard deviation of the ‘Trans-eq acc’.

Item Acc	Seen		Unseen	
	Baseline	Ours	Baseline	Ours
img, quad1	0.856 (0.005)	0.877 (0.006)	0.685 (0.042)	0.814 (0.033)
img, quad4	0.826 (0.005)	0.854 (0.004)	0.467 (0.041)	0.628 (0.058)
text, quad1	0.952 (0.004)	0.959 (0.001)	0.418 (0.006)	0.478 (0.036)
text, quad4	0.952 (0.005)	0.950 (0.001)	0.239 (0.027)	0.295 (0.018)

Table 8. Item accuracy of generated fashion images and texts in Quad1 & Quad4.

we report increased image and text generation performance of TE-VQGAN for ‘Unseen’ samples. The item accuracy for Quad2 and Quad3, color accuracy, and generated samples are provided in Appendix D.5.

## 5. Discussion

*The original or primary colours are red, yellow, green, blue and violet-purple, together with orange, indigo... Isaac Newton, 1671 [20].*

The first person to divide rainbow into 7 colors was Sir Isaac Newton. It is known that up to 207 colors of rainbows can be distinguished by human eye, but Newton expressed rainbows with only seven ‘essences’. Our methodology is similar in spirit: using the orthogonality regularization, only a few essence codebook embedding vectors are used as described in Fig. 1. We counted the number of codes that are used at least once in Stage 1. In Tab. 9,

Dataset	Baseline	Ours
MNIST	252	14
FASHION	250	18

Table 9. Code usage comparison between ‘Baseline’ and ‘Ours’.

‘Baseline’ and ‘Ours’ denote VQGAN without and with orthogonality, respectively. Both experiments were conducted fixing all other factors: SC downsampling method, and 256 codebook size, etc. Surprisingly, VQGAN with orthogonality (‘Ours’) used only 14 and 18 codes to represent colored digits and colored fashion items. In other words, the 14 and 18 ‘essence’ codes were sufficient to represent each dataset, which lead to a lower training loss during Stage 2 (training curve provided in Appendix D.1).

Since our method uses fewer codes, we posit that the Stage 2 generator would be able to learn the relationship between image and text even with a smaller dataset. Therefore, we conducted an additional experiment where we trained two *Bi-directional DALL-E*’s with a small (100K) and large train set (300K). Then we measured the two generators’ digit accuracy of T → I generation using the ‘Unseen’ test

Size	Baseline	Ours
300K	0.812 (0.032)	0.931 (0.033)
100K	0.739 (0.037)	0.919 (0.022)
Diff	0.073	0.012

Table 10. We measured Quad1 digit accuracy of T → I generation using MNIST dataset varying the size of the train set.

Dataset	Recon loss		Perceptual loss	
	Baseline	Ours	Baseline	Ours
MNIST	0.0079	0.0084	0.0036	0.0048
FASHION	0.0150	0.0187	0.0108	0.0198

Table 11. Reconstruction loss and perceptual loss [38].

set. We fixed all other factors: SC downsampling method, and 128 codebook size, etc. Tab. 10 shows that the generator with TE-VQGAN is more robust to the decrease in train set size than the generator with vanilla VQGAN.

One possible limitation of using fewer ‘essence’ codes is sacrifice in image fidelity. Drawing a rainbow with only 7 colors will certainly miss its finer hue. Tab. 11 shows the reconstruction loss  $\|\mathbf{x} - \hat{\mathbf{x}}\|_1$  and the perceptual loss [38] between input image  $\mathbf{x}$  and reconstructed image  $\hat{\mathbf{x}}$ . This empirically confirms that, even though orthogonal regularization does miss some visual information, its impact is marginal.

We also qualitatively analyzed the input images and the reconstructed images as shown in Appendix D.6. Reconstructed images in Appendix D.6 suggest that the reconstruction quality is on par with the original VQGAN while using a very small number of codes, losing only minor details. Since our ultimate aim lies in multimodal generation (e.g., text-to-image, and image-to-text) rather than reconstructing images, the ability of understanding the semantics of the given condition is more important than reconstructing every bit of fine details. Therefore, considering the result from Sec. 4.2, we can conclude that despite some minor drawbacks, we can achieve more desirable goal of multimodal generation.<sup>2</sup>

## 6. Conclusion

In this work, we first explored *translation equivariance in the image quantized space* and proposed a simple and effective way to achieve it. We empirically showed that our method increased translation equivariance, which lead to increased image-text multimodal generation performance. Future research directions include a large-scale analysis of other image quantizers regarding training with orthogonality regularization and the corresponding performance in multiple downstream tasks.

<sup>2</sup>This quantitative and qualitative analysis on the CUB-200 [32] birds dataset is in Appendix E.



## References

- [1] Aharon Azulay and Yair Weiss. Why do deep convolutional networks generalize so poorly to small image transformations? *arXiv preprint arXiv:1805.12177*, 2018. [2](#), [6](#)
- [2] Tadas Baltrušaitis, Chaitanya Ahuja, and Louis-Philippe Morency. Multimodal machine learning: A survey and taxonomy. *IEEE transactions on pattern analysis and machine intelligence*, 41(2):423–443, 2018. [2](#)
- [3] Nitin Bansal, Xiaohan Chen, and Zhangyang Wang. Can we gain more from orthogonality regularizations in training deep cnns? *arXiv preprint arXiv:1810.09102*, 2018. [4](#)
- [4] Mark Chen, Alec Radford, Rewon Child, Jeffrey Wu, Heewoo Jun, David Luan, and Ilya Sutskever. Generative pre-training from pixels. In *International Conference on Machine Learning*, pages 1691–1703. PMLR, 2020. [1](#)
- [5] Jaemin Cho, Jiasen Lu, Dustin Schwenk, Hannaneh Hajishirzi, and Aniruddha Kembhavi. X-lxmert: Paint, caption and answer questions with multi-modal transformers. *arXiv preprint arXiv:2009.11278*, 2020. [3](#)
- [6] Alexey Dosovitskiy, Lucas Beyer, Alexander Kolesnikov, Dirk Weissenborn, Xiaohua Zhai, Thomas Unterthiner, Mostafa Dehghani, Matthias Minderer, Georg Heigold, Sylvain Gelly, et al. An image is worth 16x16 words: Transformers for image recognition at scale. *arXiv preprint arXiv:2010.11929*, 2020. [2](#)
- [7] Patrick Esser, Robin Rombach, and Bjorn Ommer. Taming transformers for high-resolution image synthesis. In *Proceedings of the IEEE/CVF Conference on Computer Vision and Pattern Recognition*, pages 12873–12883, 2021. [1](#), [2](#), [3](#)
- [8] Angela Fan, Mike Lewis, and Yann Dauphin. Hierarchical neural story generation. *arXiv preprint arXiv:1805.04833*, 2018. [7](#)
- [9] Jonas Gehring, Michael Auli, David Grangier, Denis Yarats, and Yann N Dauphin. Convolutional sequence to sequence learning. In *International Conference on Machine Learning*, pages 1243–1252. PMLR, 2017. [4](#)
- [10] Rafael C Gonzalez, Richard E Woods, et al. Digital image processing, 2002. [2](#)
- [11] Kaiming He, Xiangyu Zhang, Shaoqing Ren, and Jian Sun. Deep residual learning for image recognition. In *Proceedings of the IEEE conference on computer vision and pattern recognition*, pages 770–778, 2016. [6](#)
- [12] Yupan Huang, Hongwei Xue, Bei Liu, and Yutong Lu. Unifying multimodal transformer for bi-directional image and text generation. In *Proceedings of the 29th ACM International Conference on Multimedia*, pages 1138–1147, 2021. [3](#)
- [13] Phillip Isola, Jun-Yan Zhu, Tinghui Zhou, and Alexei A Efros. Image-to-image translation with conditional adversarial networks. In *Proceedings of the IEEE conference on computer vision and pattern recognition*, pages 1125–1134, 2017. [3](#)
- [14] Tero Karras, Miika Aittala, Samuli Laine, Erik Härkönen, Janne Hellsten, Jaakko Lehtinen, and Timo Aila. Alias-free generative adversarial networks. *arXiv preprint arXiv:2106.12423*, 2021. [2](#), [6](#)
- [15] Diederik P Kingma and Jimmy Ba. Adam: A method for stochastic optimization. *arXiv preprint arXiv:1412.6980*, 2014. [5](#), [6](#)
- [16] Guang Li, Linchao Zhu, Ping Liu, and Yi Yang. Entangled transformer for image captioning. In *Proceedings of the IEEE/CVF International Conference on Computer Vision*, pages 8928–8937, 2019. [3](#)
- [17] Xiujun Li, Xi Yin, Chunyuan Li, Pengchuan Zhang, Xiaowei Hu, Lei Zhang, Lijuan Wang, Houdong Hu, Li Dong, Furu Wei, et al. Oscar: Object-semantics aligned pre-training for vision-language tasks. In *European Conference on Computer Vision*, pages 121–137. Springer, 2020. [3](#)
- [18] Wei Liu, Sihan Chen, Longteng Guo, Xinxin Zhu, and Jing Liu. Cptr: Full transformer network for image captioning. *arXiv preprint arXiv:2101.10804*, 2021. [3](#)
- [19] Ilya Loshchilov and Frank Hutter. Sgdr: Stochastic gradient descent with warm restarts. *arXiv preprint arXiv:1608.03983*, 2016. [6](#)
- [20] Isaac Newton. A letter of mr. isaac newton, professor of the mathematicks in the university of cambridge; containing his new theory about light and colors: sent by the author to the publisher from cambridge, febr. 6. 1671/72; in order to be communicated to the r. society. *Philosophical Transactions of the Royal Society of London*, 6(80):3075–3087, 2014. [8](#)
- [21] Harry Nyquist. Certain topics in telegraph transmission theory. *Transactions of the American Institute of Electrical Engineers*, 47(2):617–644, 1928. [2](#)
- [22] Aaron van den Oord, Nal Kalchbrenner, Oriol Vinyals, Lasse Espeholt, Alex Graves, and Koray Kavukcuoglu. Conditional image generation with pixelcnn decoders. *arXiv preprint arXiv:1606.05328*, 2016. [1](#)
- [23] Alan V Oppenheim. *Discrete-time signal processing*. Pearson Education India, 1999. [2](#)
- [24] Adam Paszke, Sam Gross, Francisco Massa, Adam Lerer, James Bradbury, Gregory Chanan, Trevor Killeen, Zeming Lin, Natalia Gimelshein, Luca Antiga, et al. Pytorch: An imperative style, high-performance deep learning library. *Advances in neural information processing systems*, 32:8026–8037, 2019. [5](#)
- [25] Aditya Ramesh, Mikhail Pavlov, Gabriel Goh, Scott Gray, Chelsea Voss, Alec Radford, Mark Chen, and Ilya Sutskever. Zero-shot text-to-image generation. *arXiv preprint arXiv:2102.12092*, 2021. [1](#), [3](#), [4](#)
- [26] Rico Sennrich, Barry Haddow, and Alexandra Birch. Neural machine translation of rare words with subword units. *arXiv preprint arXiv:1508.07909*, 2015. [4](#), [6](#)
- [27] Eero P Simoncelli, William T Freeman, Edward H Adelson, and David J Heeger. Shiftable multiscale transforms. *IEEE transactions on Information Theory*, 38(2):587–607, 1992. [2](#)
- [28] Aäron van den Oord, Oriol Vinyals, and Koray Kavukcuoglu. Neural discrete representation learning. In *NIPS*, 2017. [1](#), [2](#), [3](#), [5](#)
- [29] Aaron Van Oord, Nal Kalchbrenner, and Koray Kavukcuoglu. Pixel recurrent neural networks. In *International Conference on Machine Learning*, pages 1747–1756. PMLR, 2016. [1](#)

- [30] Cristina Vasconcelos, Hugo Larochelle, Vincent Dumoulin, Rob Romijnders, Nicolas Le Roux, and Ross Goroshin. Impact of aliasing on generalization in deep convolutional networks. In *Proceedings of the IEEE/CVF International Conference on Computer Vision*, pages 10529–10538, 2021. [2](#)
- [31] Ashish Vaswani, Noam Shazeer, Niki Parmar, Jakob Uszkoreit, Llion Jones, Aidan N Gomez, Łukasz Kaiser, and Illia Polosukhin. Attention is all you need. In *Advances in neural information processing systems*, pages 5998–6008, 2017. [1](#)
- [32] Catherine Wah, Steve Branson, Peter Welinder, Pietro Perona, and Serge Belongie. The caltech-ucsd birds-200-2011 dataset. 2011. [8](#), [13](#)
- [33] Zelun Wang and Jyh-Charn Liu. Translating math formula images to latex sequences using deep neural networks with sequence-level training. *International Journal on Document Analysis and Recognition (IJDAR)*, 24(1):63–75, 2021. [4](#)
- [34] Han Xiao, Kashif Rasul, and Roland Vollgraf. Fashion-mnist: a novel image dataset for benchmarking machine learning algorithms. *arXiv preprint arXiv:1708.07747*, 2017. [7](#)
- [35] Xu Yang, Hanwang Zhang, and Jianfei Cai. Learning to collocate neural modules for image captioning. In *Proceedings of the IEEE/CVF International Conference on Computer Vision*, pages 4250–4260, 2019. [3](#)
- [36] Jiahui Yu, Xin Li, Jing Yu Koh, Han Zhang, Ruoming Pang, James Qin, Alexander Ku, Yuanzhong Xu, Jason Baldridge, and Yonghui Wu. Vector-quantized image modeling with improved vqgan. *arXiv preprint arXiv:2110.04627*, 2021. [2](#)
- [37] Richard Zhang. Making convolutional networks shift-invariant again. In *International conference on machine learning*, pages 7324–7334. PMLR, 2019. [2](#), [5](#), [6](#)
- [38] Richard Zhang, Phillip Isola, Alexei A Efros, Eli Shechtman, and Oliver Wang. The unreasonable effectiveness of deep features as a perceptual metric. In *Proceedings of the IEEE conference on computer vision and pattern recognition*, pages 586–595, 2018. [3](#), [8](#), [14](#)
- [39] Luowei Zhou, Hamid Palangi, Lei Zhang, Houdong Hu, Jason Corso, and Jianfeng Gao. Unified vision-language pre-training for image captioning and vqa. In *Proceedings of the AAAI Conference on Artificial Intelligence*, volume 34, pages 13041–13049, 2020. [3](#)
- [40] Xueyan Zou, Fanyi Xiao, Zhiding Yu, and Yong Jae Lee. Delving deeper into anti-aliasing in convnets. *arXiv preprint arXiv:2008.09604*, 2020. [2](#)

## A. Training Details

All experiments are conducted on RTX 3090 GPUs. In Stage 1, the batch size is set to 96 on a GPU with 24GB VRAM, and we trained each VQGAN using 2 GPUs (*i.e.*, total batch size is  $96 \times 2 = 192$ ). Further note that GAN loss  $\mathcal{L}_{GAN}$  in Eq. (1) works after 30,000 steps for warming up the VQGAN’s generator (encoder  $\mathcal{F}$ , decoder  $\mathcal{G}$ , embedding  $e$ ). In Stage 2, the batch size is set to 100 on a GPU, and each *Bi-directional DALL-E* is trained with 2 GPUs (*i.e.*, total batch size is  $100 \times 2 = 200$ ). We clipped the gradient norm to 1.0 to prevent the gradient exploding, and the attention mask types for bi-directional image-text generation are illustrated in Fig. 6. All of the codes in this work are written in PyTorch 1.7.1.

## B. Dataset Examples

Some examples of *Stage 1 Dataset* and *Translated Dataset* are illustrated in Fig. 7 and Fig. 8, respectively. Fig. 9 and Fig. 10 also show some examples of *Stage 2 Dataset* (test set) for MNIST and fashion-MNIST, respectively.

## C. Enforcing Codebook Norm to be 1

There are two cases of the orthogonality regularization terms depending on whether we are going to enforce the codebook embedding norm to be 1:

$$\lambda \frac{1}{K^2} \|e^\top e - I\|_F^2 \quad (5)$$

$$\lambda \frac{1}{K^2} \|\ell_2(e)^\top \ell_2(e) - I\|_F^2 \quad (6)$$

where  $e \in \mathbb{R}^{C' \times K}$  denotes the codebook embeddings, and  $\ell_2(e) \in \mathbb{R}^{C' \times K}$  denotes the  $L_2$ -normalized codebook embeddings along the first dimension. Note that Eq. (5) enforces the norm of the codebook embedding vector  $e_i \in \mathbb{R}^{C'}$  to be 1.

Case	MIN(norm)	MAX(norm)	Trans-eq acc
Eq. (5)	0.999	1.114	0.815 (0.021)
Eq. (6)	2.047	22.495	0.970 (0.010)

Table 12. Results of the two cases. ‘MIN(norm)’ and ‘MAX(norm)’ denotes the minimum and maximum norm among  $K$  codebook embeddings, respectively.

We tested the above two cases with using 128 codebook size and SC downsampling method. If we enforces the norm of the codebook embedding vectors to be 1 (the case of Eq. (5)), the norm of the codebook embedding vectors are indeed between 0.999 and 1.114. However, enforcing the norm to be 1 is not effective in terms of ‘Trans-eq acc’.

## D. Additional Results

### D.1. Loss curve

The Stage 2 model with our TE-VQGAN reaches a lower training loss in the both tasks, as shown in Fig. 11.

### D.2. MNIST: T $\rightarrow$ I Generation

Tab. 13 and Tab. 14 show digit accuracy of generated images for Quad2 and Quad3, respectively. Also color accuracy of generated images is reported in Tab. 15.

Quad2	Seen		Unseen	
	Baseline	Ours	Baseline	Ours
SC	0.926 (0.015)	0.955 (0.007)	0.806 (0.030)	0.913 (0.032)
CB	0.948 (0.010)	0.959 (0.004)	0.741 (0.034)	0.919 (0.014)
MP	0.944 (0.008)	0.957 (0.011)	0.703 (0.015)	0.906 (0.077)
MB	0.931 (0.025)	0.920 (0.005)	0.697 (0.066)	0.858 (0.020)

Table 13. Digit accuracy of generated images in Quad2.

Quad3	Seen		Unseen	
	Baseline	Ours	Baseline	Ours
SC	0.924 (0.004)	0.954 (0.013)	0.790 (0.038)	0.890 (0.048)
CB	0.938 (0.012)	0.958 (0.009)	0.682 (0.043)	0.895 (0.049)
MP	0.942 (0.005)	0.961 (0.009)	0.669 (0.017)	0.880 (0.087)
MB	0.924 (0.026)	0.911 (0.010)	0.635 (0.067)	0.796 (0.023)

Table 14. Digit accuracy of generated images in Quad3.

	Seen		Unseen	
	Baseline	Ours	Baseline	Ours
SC, Quad1	0.999 (0.001)	0.994 (0.002)	0.998 (0.002)	0.996 (0.001)
CB, Quad1	0.999 (0.001)	0.993 (0.003)	0.999 (0.001)	0.970 (0.007)
MP, Quad1	0.999 (0.001)	0.994 (0.004)	0.998 (0.003)	0.984 (0.003)
MB, Quad1	0.999 (0.001)	0.997 (0.002)	0.998 (0.002)	0.994 (0.004)
SC, Quad2	0.999 (0.001)	0.996 (0.001)	0.999 (0.001)	0.991 (0.004)
CB, Quad2	0.999 (0.001)	0.996 (0.003)	0.998 (0.001)	0.975 (0.012)
MP, Quad2	0.999 (0.001)	0.997 (0.001)	0.994 (0.004)	0.982 (0.006)
MB, Quad2	0.999 (0.001)	0.998 (0.001)	0.999 (0.001)	0.996 (0.001)
SC, Quad3	0.999 (0.001)	0.996 (0.002)	0.997 (0.004)	0.992 (0.004)
CB, Quad3	0.999 (0.001)	0.996 (0.001)	0.998 (0.002)	0.969 (0.024)
MP, Quad3	0.999 (0.001)	0.994 (0.001)	0.991 (0.011)	0.978 (0.015)
MB, Quad3	0.999 (0.001)	0.998 (0.001)	0.997 (0.002)	0.991 (0.002)
SC, Quad4	0.998 (0.001)	0.996 (0.003)	0.997 (0.003)	0.990 (0.006)
CB, Quad4	0.999 (0.001)	0.997 (0.001)	0.998 (0.002)	0.972 (0.021)
MP, Quad4	0.999 (0.001)	0.992 (0.001)	0.991 (0.011)	0.974 (0.021)
MB, Quad4	0.999 (0.001)	0.995 (0.002)	0.998 (0.002)	0.994 (0.002)

Table 15. Color accuracy of generated images.

### D.3. MNIST: I $\rightarrow$ T Generation

Similar to T  $\rightarrow$  I generation, we reported digit accuracy of generated texts for Quad2 and Quad3 in Tab. 16 and Tab. 17, respectively. Color accuracy of generated texts is reported in Tab. 18.

### D.4. MNIST: Generated Samples

The generated samples by *Bi-directional DALL-E* with our TE-VQGAN are shown in Fig. 12.

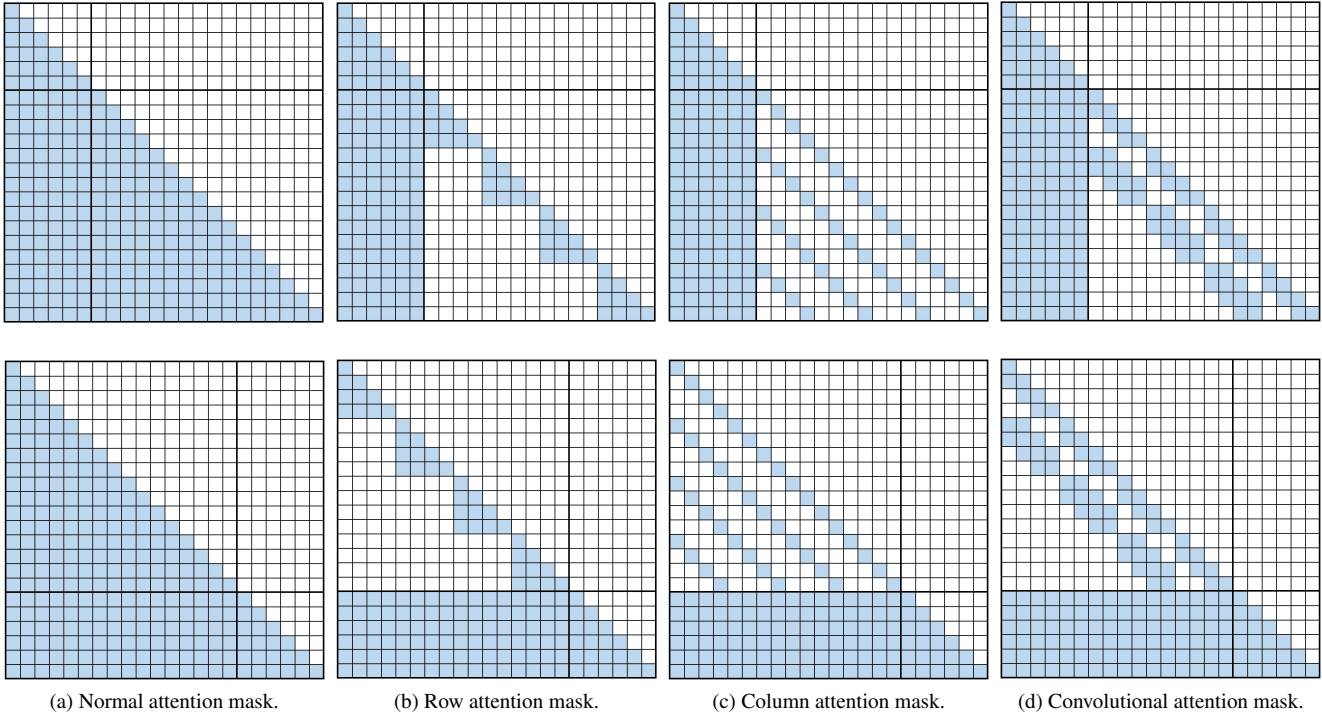


Figure 6. Illustration of the four types of attention masks with a maximum text length of 6 tokens and image length of 16 tokens (*i.e.*,  $4 \times 4$  grid). The first and second row indicate the attention mask types of  $T \rightarrow I$  and  $I \rightarrow T$  generation, respectively. Every four self-attention layers use the normal, row, column, convolutional attention mask, respectively. For example, the first layer adopts the normal attention mask, the second layer adopts the row attention mask, and so on.

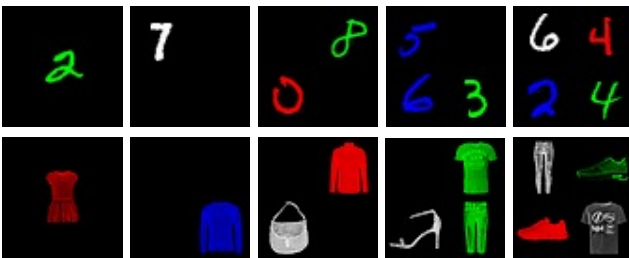


Figure 7. Stage 1 Dataset.

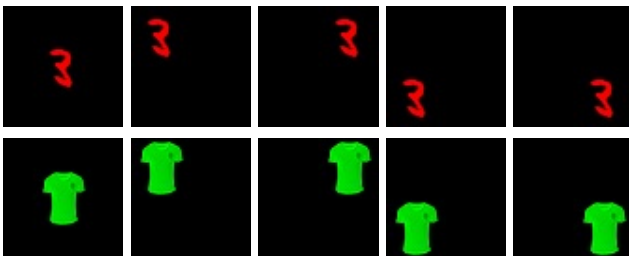


Figure 8. Translated Dataset.

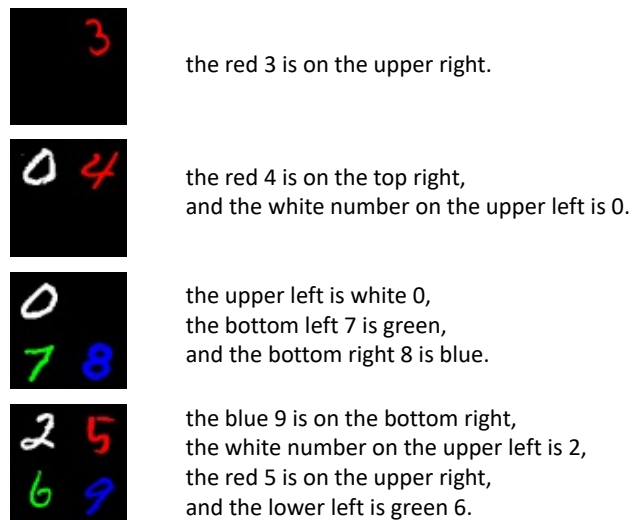


Figure 9. MNIST Stage 2 Dataset (test set).

### D.5. Fashion-MNIST: $T \rightarrow I$ & $I \rightarrow T$ Generation

Similar to MNIST, we reported item accuracy and color accuracy for the both tasks in Tab. 19 and Tab. 20, respectively. The generated samples by *Bi-directional DALL-E* with our TE-VQGAN are shown in Fig. 13.



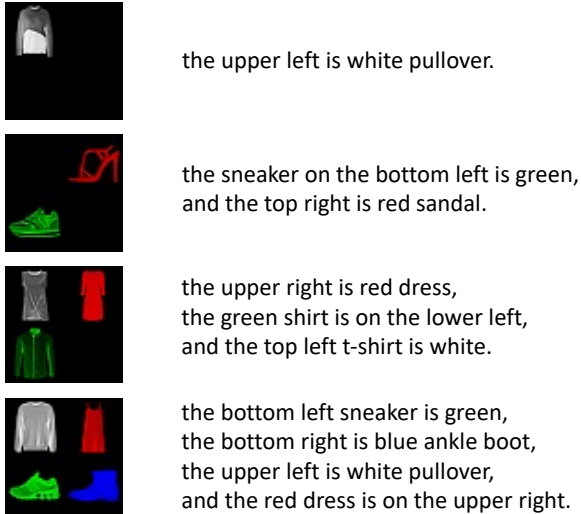


Figure 10. FASHION Stage 2 Dataset (test set).

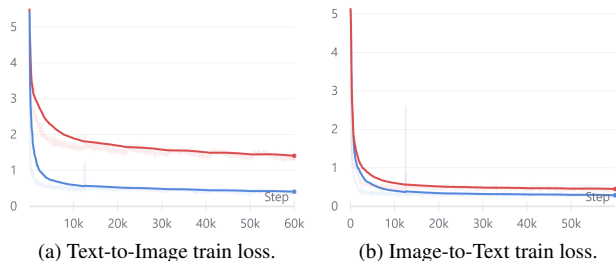


Figure 11. Stage 2 training loss for MNIST dataset. Blue line and red line denote the Stage 2 generator with TE-VQGAN and with vanilla VQGAN, respectively.

Quad2	Seen		Unseen	
	Baseline	Ours	Baseline	Ours
SC	0.990 (0.001)	0.987 (0.004)	0.545 (0.009)	0.662 (0.084)
CB	0.992 (0.002)	0.991 (0.001)	0.372 (0.021)	0.440 (0.068)
MP	0.992 (0.003)	0.990 (0.001)	0.417 (0.023)	0.480 (0.052)
MB	0.995 (0.002)	0.990 (0.002)	0.418 (0.078)	0.621 (0.049)

Table 16. Digit accuracy of generated texts in Quad2.

Quad3	Seen		Unseen	
	Baseline	Ours	Baseline	Ours
SC	0.989 (0.003)	0.987 (0.001)	0.453 (0.017)	0.562 (0.080)
CB	0.992 (0.003)	0.993 (0.002)	0.291 (0.021)	0.385 (0.040)
MP	0.990 (0.003)	0.991 (0.003)	0.337 (0.026)	0.416 (0.059)
MB	0.993 (0.001)	0.989 (0.001)	0.348 (0.077)	0.512 (0.034)

Table 17. Digit accuracy of generated texts in Quad3.

## D.6. Reconstructed Images

Fig. 14 shows the comparison of reconstruction quality between vanilla VQGAN and TE-VQGAN for MNIST and fashion-MNIST dataset.

	Seen		Unseen	
	Baseline	Ours	Baseline	Ours
SC, Quad1	0.999 (0.001)	0.999 (0.001)	0.989 (0.016)	0.990 (0.004)
CB, Quad1	0.999 (0.001)	0.998 (0.001)	0.990 (0.007)	0.987 (0.017)
MP, Quad1	0.999 (0.001)	0.999 (0.001)	0.973 (0.004)	0.995 (0.003)
MB, Quad1	0.999 (0.001)	0.998 (0.001)	0.986 (0.012)	0.973 (0.032)
SC, Quad2	0.999 (0.001)	0.998 (0.001)	0.985 (0.008)	0.990 (0.002)
CB, Quad2	0.999 (0.001)	0.999 (0.001)	0.991 (0.001)	0.985 (0.016)
MP, Quad2	0.999 (0.001)	0.999 (0.001)	0.986 (0.007)	0.992 (0.007)
MB, Quad2	0.999 (0.001)	0.999 (0.001)	0.988 (0.008)	0.986 (0.009)
SC, Quad3	0.999 (0.001)	0.999 (0.001)	0.989 (0.001)	0.989 (0.005)
CB, Quad3	0.999 (0.001)	0.999 (0.001)	0.995 (0.002)	0.993 (0.004)
MP, Quad3	0.999 (0.001)	0.999 (0.001)	0.992 (0.005)	0.994 (0.002)
MB, Quad3	0.999 (0.001)	0.998 (0.001)	0.991 (0.007)	0.990 (0.005)
SC, Quad4	0.996 (0.005)	0.997 (0.004)	0.987 (0.003)	0.988 (0.001)
CB, Quad4	0.999 (0.001)	0.999 (0.001)	0.995 (0.001)	0.995 (0.001)
MP, Quad4	0.999 (0.001)	0.998 (0.001)	0.991 (0.001)	0.993 (0.004)
MB, Quad4	0.999 (0.001)	0.998 (0.001)	0.994 (0.002)	0.991 (0.005)

Table 18. Color accuracy of generated texts.

Item Acc	Seen		Unseen	
	Baseline	Ours	Baseline	Ours
img, Quad2	0.832 (0.005)	0.858 (0.004)	0.603 (0.044)	0.735 (0.033)
img, Quad3	0.833 (0.004)	0.859 (0.002)	0.538 (0.041)	0.691 (0.051)
text, Quad2	0.949 (0.004)	0.946 (0.005)	0.297 (0.016)	0.359 (0.016)
text, Quad3	0.946 (0.005)	0.947 (0.005)	0.279 (0.027)	0.340 (0.017)

Table 19. Item accuracy of generated fashion images and texts in Quad2 & Quad3.

Color Acc	Seen		Unseen	
	Baseline	Ours	Baseline	Ours
img, Quad1	0.998 (0.003)	0.997 (0.002)	0.997 (0.001)	0.997 (0.001)
img, Quad2	0.999 (0.001)	0.997 (0.002)	0.997 (0.003)	0.994 (0.001)
img, Quad3	0.999 (0.001)	0.997 (0.001)	0.993 (0.006)	0.988 (0.001)
img, Quad4	0.998 (0.001)	0.997 (0.002)	0.992 (0.005)	0.985 (0.004)
text, Quad1	0.999 (0.001)	0.999 (0.001)	0.990 (0.006)	0.996 (0.002)
text, Quad2	0.999 (0.001)	0.999 (0.001)	0.992 (0.003)	0.994 (0.001)
text, Quad3	0.999 (0.001)	0.999 (0.001)	0.993 (0.001)	0.995 (0.002)
text, Quad4	0.998 (0.001)	0.998 (0.001)	0.989 (0.007)	0.994 (0.002)

Table 20. Color accuracy of generated fashion images and texts.

## E. Additional Dataset: CUB-200

We conducted similar experiments in Stage 1 on another dataset, CUB-200 [32]. We constructed our bird dataset of  $256 \times 256$  resolution without background similar to our *Stage 1 Dataset*. Note that the original CUB-200 dataset has 11,788 images, and we split them into 10,000 for train set and 1,788 for test set. We constructed our train set of size 50,000 by combining the 10,000 images and test set of size 8,940 by combining the 1,788 images. We fixed the downsampling method to SC and the codebook size to 256, and measured the performance of translation equivariance as shown in Tab. 21. We also reported the number of codes that are used at least once for our 8,940 test set images (Tab. 23). The comparison of reconstruction quality between vanilla VQGAN and TE-VQGAN is reported in Tab. 22 and Fig. 15.

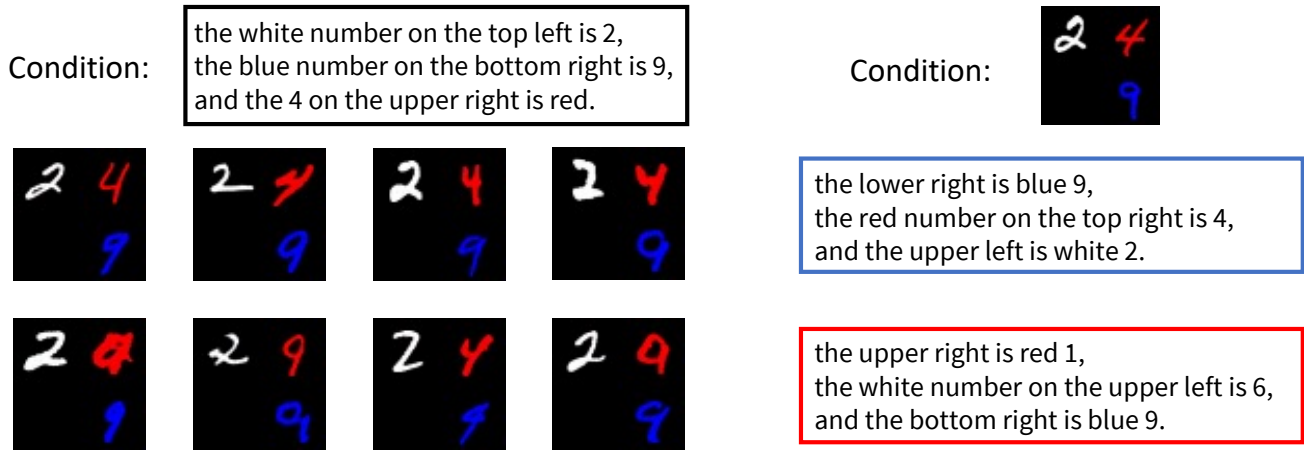


Figure 12. Generated samples by the Stage 2 model with our TE-VQGAN for MNIST dataset. In this example, TE-VQGAN is set to SC downsampling method and 128 codebook size. The first, second, and third row indicate the condition as input, correctly generated samples, and incorrectly generated samples, respectively.

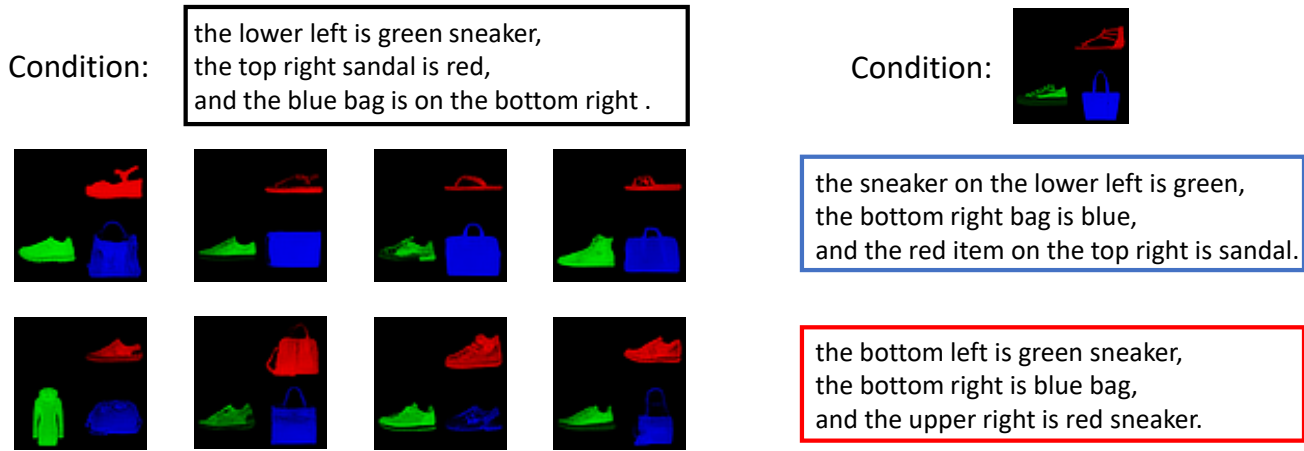


Figure 13. Generated samples by the Stage 2 model with our TE-VQGAN for fashion-MNIST dataset. In this example, TE-VQGAN is set to SC downsampling method and 128 codebook size. The first, second, and third row indicate the condition as input, correctly generated samples, and incorrectly generated samples, respectively.

	Baseline	Ours
SC, 256	0.796 (0.016)	0.898 (0.013)

Table 21. Mean and standard deviation of ‘Trans-eq acc’. We used SC downsampling method and 256 codebook embeddings.

Dataset	Recon loss		Perceptual loss	
	Baseline	Ours	Baseline	Ours
BIRD	0.0297	0.0329	0.0728	0.0768

Table 22. Reconstruction loss and perceptual loss [38].

Dataset	Baseline	Ours
BIRD	125	63

Table 23. Code usage comparison between ‘Baseline’ and ‘Ours’.

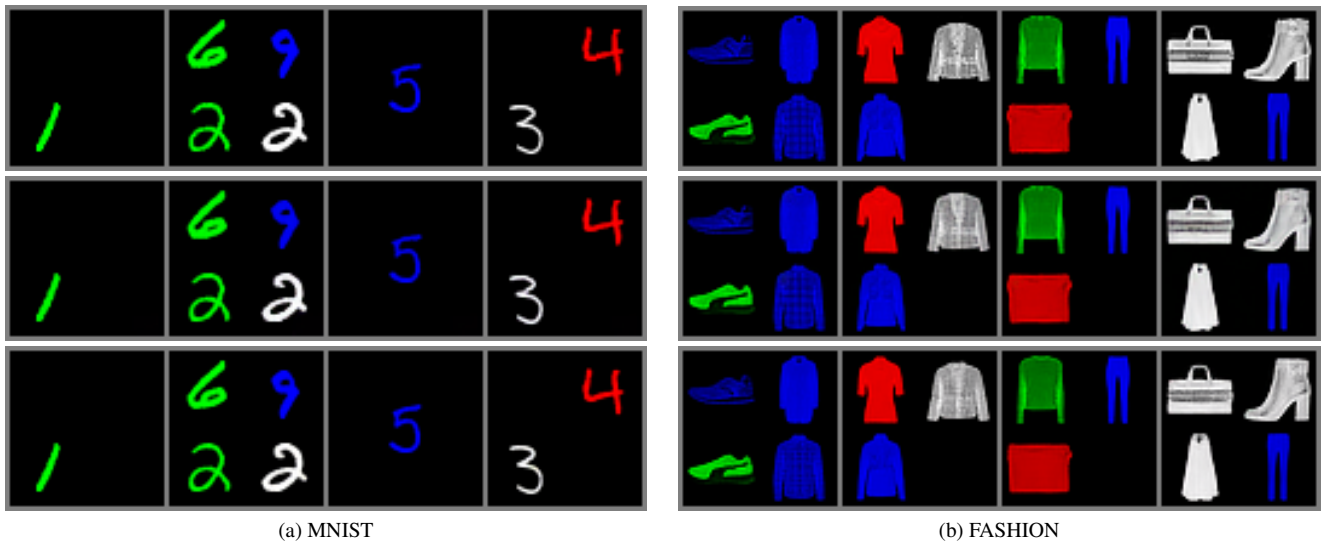


Figure 14. The first, second, and third row indicate input images, reconstructed images of vanilla VQGAN, and reconstructed images of TE-VQGAN, respectively.



Figure 15. The first, second, and third row indicate input images, reconstructed images of vanilla VQGAN, and reconstructed images of TE-VQGAN, respectively.